






# Plastic and low-cost axial zero thermal expansion alloy by a natural dual-phase composite

Chengyi Yu<sup>1</sup>, Kun Lin<sup>1</sup>  <sup>✉</sup>, Suihe Jiang<sup>1</sup> , Yili Cao<sup>1</sup>, Wenjie Li<sup>1</sup>, Yilin Wang<sup>1</sup>, Yan Chen<sup>2</sup>, Ke An<sup>2</sup> , Li You<sup>1</sup>, Kenichi Kato<sup>3</sup>, Qiang Li<sup>1</sup>, Jun Chen<sup>1</sup> , Jinxia Deng<sup>1</sup> & Xianran Xing<sup>1</sup>  <sup>✉</sup>

Zero thermal expansion (ZTE) alloys possess unique dimensional stability, high thermal and electrical conductivities. Their practical application under heat and stress is however limited by their inherent brittleness because ZTE and plasticity are generally exclusive in a single-phase material. Besides, the performance of ZTE alloys is highly sensitive to change of compositions, so conventional synthesis methods such as alloying or the design of multi-phase to improve its thermal and mechanical properties are usually inapplicable. In this study, by adopting a one-step eutectic reaction method, we overcome this challenge. A natural dual-phase composite with ZTE and plasticity was synthesized by melting 4 atom% holmium with pure iron. The dual-phase alloy shows moderate plasticity and strength, axial zero thermal expansion, and stable thermal cycling performance as well as low cost. By using synchrotron X-ray diffraction, in-situ neutron diffraction and microscopy, the critical mechanism of dual-phase synergy on both thermal expansion regulation and mechanical property enhancement is revealed. These results demonstrate that eutectic reaction is likely to be a universal and effective method for the design of high-performance intermetallic-compound-based ZTE alloys.

<sup>1</sup> Beijing Advanced Innovation Center for Materials Genome Engineering, Institute of Solid State Chemistry, Department of Physical Chemistry, University of Science and Technology Beijing, Beijing, China. <sup>2</sup> Neutron Scattering Division, Oak Ridge National Laboratory, Oak Ridge, TN, USA. <sup>3</sup> RIKEN SPring-8 Center, Hyogo, Japan. ✉email: [kunlin@ustb.edu.cn](mailto:kunlin@ustb.edu.cn); [xing@ustb.edu.cn](mailto:xing@ustb.edu.cn)

Zero thermal expansion (ZTE) alloy plays an important role in our daily life ranging from mechanical watches to communication satellites because of its size-stability under temperature fluctuations<sup>1–3</sup>. However, ZTE material is rare in nature. This behavior is especially unusual for metallic materials. Only a few couplings among lattice, spin, and orbital induce a reduced coefficient of thermal expansion by the virtue of the so-called magneto-volume effect<sup>4–6</sup>, which has been reported in a few single-phase metallic materials, such as the conventional Invar alloy<sup>7</sup> ( $\text{Fe}_{0.64}\text{Ni}_{0.36}$ ) and some magnetic intermetallic compounds (e.g.,  $\text{Tb}(\text{Co},\text{Fe})_2$ <sup>8</sup>,  $\text{La}(\text{Fe},\text{Si},\text{Co})_{13}$ <sup>9</sup>). On the other hand, most of these ZTE compounds are brittle with low strength and little ductility<sup>10–14</sup>, with concerned applicability due to low fracture toughness. It is noted here that the widely used Invar alloy shows plasticity but with low strength. An alternative way to design ZTE alloys is to mix thermal expansion material with thermal contraction one (e.g.,  $\text{La}(\text{Fe},\text{Si})_{13}/\text{Cu}$ <sup>15</sup> and  $\text{ZrW}_2\text{O}_8/\text{Al}$ <sup>16</sup>). But these artificial composites usually suffer from undesired microstructures or weak interfacial bonding, resulting in poor overall mechanical properties and thermal cycling performances. More importantly, the magneto-volume effect is highly composition-sensitive—a slight interfacial mass transfer during high-temperature synthesis may suppress or vanish the ZTE property<sup>5,13,17</sup>. The search for novel ZTE alloys with excellent strength-plasticity performance has been challenging for decades<sup>18–22</sup>.

In this work, we conducted a one-step strategy to design plastic and low-cost ZTE alloy by a hypo-eutectic or hyper-eutectic reaction in a binary system<sup>23–25</sup>. Iron is one of the most earth-abundant elements; its conventional phase,  $\alpha$ -Fe, has high plasticity and normal positive thermal expansion (PTE). Interestingly, on the R-Fe (R = rare earth) binary phase diagram<sup>26</sup> (see Supplementary Fig. 1), Fe forms a eutectic system with  $\text{R}_2\text{Fe}_{17}$ —a typical negative thermal expansion (NTE) intermetallic compound driven by magnetic ordering<sup>6,27,28</sup>. This indicates that the  $\text{R}_2\text{Fe}_{17}$  phase could coexist in equilibrium with Fe at any temperature without losing its own NTE character. What's more, both the phase fraction and microstructure can be easily controlled by tuning the chemical compositions in the binary system, which are key factors to thermal expansion and mechanical property improvement. Here we demonstrate that by adding only 4% Ho atoms to pure iron, an alloy with both axial ZTE ( $\text{Ho}_{0.04}\text{Fe}_{0.96}$ ,  $\alpha_1 = 0.19 \times 10^{-6} \text{ K}^{-1}$ , 100 to 335 K) could be designed and fabricated and a moderate strength-plasticity combination could be achieved. We further show that the present dual-phase alloy is highly stable under thermal circulation conditions, which is rare among alloy materials that possessed both ZTE and plasticity, and the cost-effective alloy sees great potential in applications.

## Results

**Phase and crystal structure.** The targeted samples with compositions of  $\text{Ho}_x\text{Fe}_{1-x}$  ( $x = 0.03$ ,  $x = 0.04$ ,  $x = 0.05$ ,  $x = 0.07$ ,  $x = 0.09$ , labeled as S-3 to S-9) were synthesized by traditional arc-melting. High-resolution synchrotron X-ray powder diffraction (SXRD) measurement was employed to identify the phase fractions and crystal structures. It shows that all the samples are dual-phase alloys consist of the  $\text{Ho}_2\text{Fe}_{17}$  phase (denoted as H) and  $\alpha$  iron phase (denoted as  $\alpha$ ) without other detectable impurities (see Fig. 1a). Increasing the content of Ho, the positions of Bragg peaks for both the H and  $\alpha$  phases keep almost unchanged as indicated by  $(220)_\text{H}$  and  $(110)_\alpha$  reflections in Fig. 1b, suggesting that the two phases reached thermodynamic equilibrium and can coexist in any proportion to ensure desired thermal expansion regulation. These results agree well with the Ho–Fe binary phase diagram.

Figure 1d shows the crystal structure of the H and  $\alpha$  phases refined by SXRD data. The H phase adopts  $\text{Th}_2\text{Ni}_{17}$ -type structure (space group:  $P6_3/mmc$ ) with cell parameters  $a = 8.45 \pm 0.01 \text{ \AA}$ ,  $c = 8.32 \pm 0.01 \text{ \AA}$ ,  $V = 514.09 \pm 0.03 \text{ \AA}^3$  and has six Wyckoff sites ( $\text{Ho}_{2b}$ ,  $\text{Ho}_{2d}$ ,  $\text{Fe}_{4f}$ ,  $\text{Fe}_{6g}$ ,  $\text{Fe}_{12j}$ , and  $\text{Fe}_{12k}$ ); while the  $\alpha$  phase is a body-centered-cubic phase (space group:  $I m - 3 m$ ) with cell parameters  $a = 2.87 \pm 0.00 \text{ \AA}$ ,  $V = 23.56 \pm 0.02 \text{ \AA}^3$  and has only one Wyckoff site ( $\text{Fe}_{2a}$ ). Due to a large difference in atomic radius, Ho (1.79  $\text{ \AA}$ ) and Fe (1.26  $\text{ \AA}$ ) atoms occupy separate sites in the H phase selectively: Ho atoms are surrounded by Fe atoms and form  $[\text{HoFe}_{16}]$  cages (Fig. 1d). This guarantees the structural stability of the H phase when Fe atoms can diffuse through the interface during the high-temperature synthesis. Further Rietveld refinements quantified the phase fractions of the H phases ( $29.6 \pm 0.1\%$ ,  $39.8 \pm 0.1\%$ ,  $49.8 \pm 0.1\%$ ,  $69.7 \pm 0.2\%$ , and  $86.5 \pm 0.3\%$  for S-3 to S-9, respectively, see Fig. 1c and Supplementary Fig. 2).

**Microstructure and crystallographic orientation.** Electro-probe microanalyzer (EPMA) shows that the dendritic lamellar  $\alpha$  phase (in dark, 50–100  $\mu\text{m}$ ) is homogeneously dispersed into the H phase (in white, 50–100  $\mu\text{m}$ ) matrix (see Figs. 2a–2e for S-4, see Supplementary Fig. 3 for other samples). Besides, the grains appear to grow along the loading direction (LD) (see Fig. 2b). Electron back-scattered diffraction (EBSD) inverse pole image demonstrates that the H and  $\alpha$  phases are highly textured (Fig. 2c). This is caused by the large temperature gradient and cooling rate in the cooling process, in which the phases tend to nucleate and grow along a certain direction and form bulk materials with strong anisotropy. To further investigate the lattice matching between the two phases in the bulk, neutron diffraction texture analysis was carried out. The pole figures demonstrate a strong fiber texture in the as-cast sample: the H phase is highly textured with the  $\{004\}$  grains are parallel to the loading direction (LD) while the  $\{600\}$  grains are perpendicular to LD; the  $\alpha$  phase has a less-strong orientation with  $[110]_\alpha$  roughly parallel to LD (see Fig. 2h). Consequently, the main orientation relationship between the H and  $\alpha$  phase is  $[001]_\text{H}/[110]_\alpha$ . This facilitates the formation of semi-coherent matching at the dual-phase interface and will be discussed later.

**Thermal expansion and mechanical properties.** The hexagonal H compound shows NTE but is brittle, while the bcc  $\alpha$  phase shows positive thermal expansion (PTE) and is plastic. Hence, both the coefficient of thermal expansion (CTE) and mechanical properties of the dual-phase alloys could be well controlled by adjusting phase content. Figure 3a indicates that the linear thermal expansion along LD of alloys can be successively tailored from moderate positive ( $\alpha_1 = 2.7 \times 10^{-6} \text{ K}^{-1}$ , S-3) to strong negative ( $\alpha_1 = -12.9 \times 10^{-6} \text{ K}^{-1}$ , S-9). Especially, an axial ZTE over a wide temperature range (100 to 335 K) has been obtained in S-4 alloy ( $\alpha_1 = 0.19 \times 10^{-6} \text{ K}^{-1}$ ). Such a ZTE performance demonstrates dimensional stability even under hundreds of thermal cycling conditions (see Supplementary Fig. 4 and 5). Due to the strong texture in the alloys, the CTEs in-plane (TD-ND) from S-3 to S-9 are varied from  $7.7 \times 10^{-6} \text{ K}^{-1}$  to  $-0.1 \times 10^{-6} \text{ K}^{-1}$  (see Fig. 3b). The lattice thermal expansions in the S-4 alloy were extracted by the temperature resolved SXRD, which are  $9.40 \times 10^{-6} \text{ K}^{-1}$  for  $\alpha$  phase along the  $a$  axis and  $-5.91 \times 10^{-6} \text{ K}^{-1}$  for H phase along the  $c$  axis (see Supplementary Fig. 6 and Table 2). This leads to an overall thermal expansion along the LD of the alloy to be  $1.19 \times 10^{-6} \text{ K}^{-1}$  in the temperature range of 100 to 335 K ( $\Sigma a_{S-4} = \text{mol.}\%_\alpha \times a_\alpha + \text{mol.}\%_\text{H} \times c_\text{H}$ , see Supplementary Methods), consistent with that of dilatometer measurement (see Fig. 3c). What's more, S-4 displays good plasticity during

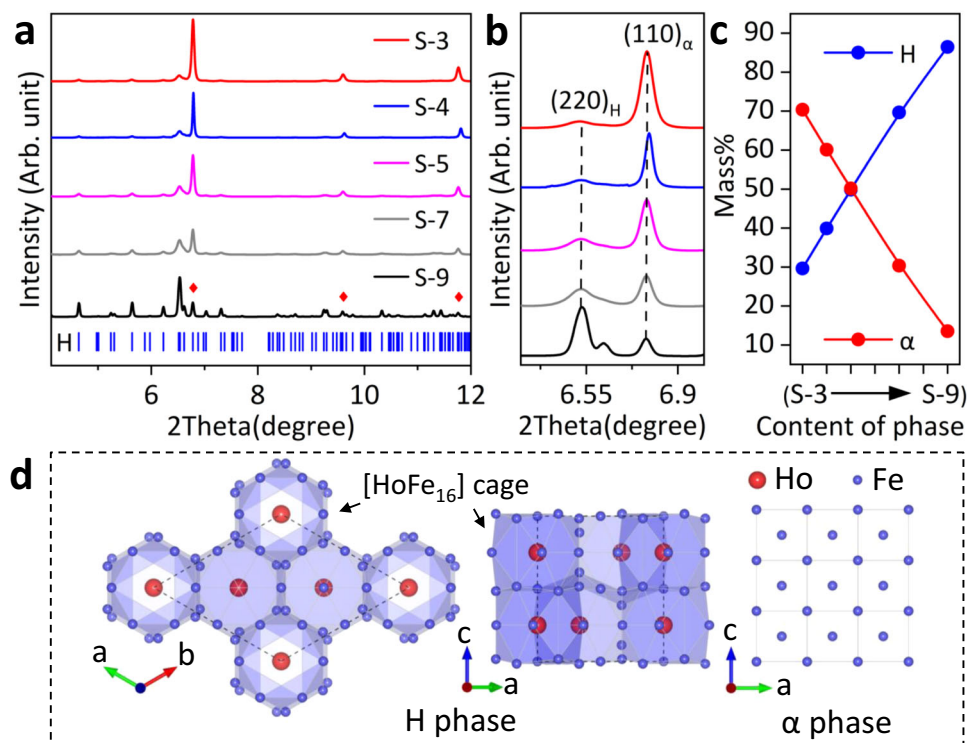


**Fig. 1** Phase and crystal structures. **a, b** High-resolution synchrotron X-ray diffraction profiles for S-3 to S-9 ( $\lambda = 0.23991 \text{ \AA}$ ), the marked red diamond is the  $\alpha$  phase. **c** The mass fractions of H and  $\alpha$  in S-3 to S-9 are determined via Rietveld refinements. **d** Crystal structures of H and  $\alpha$  phase, respectively.

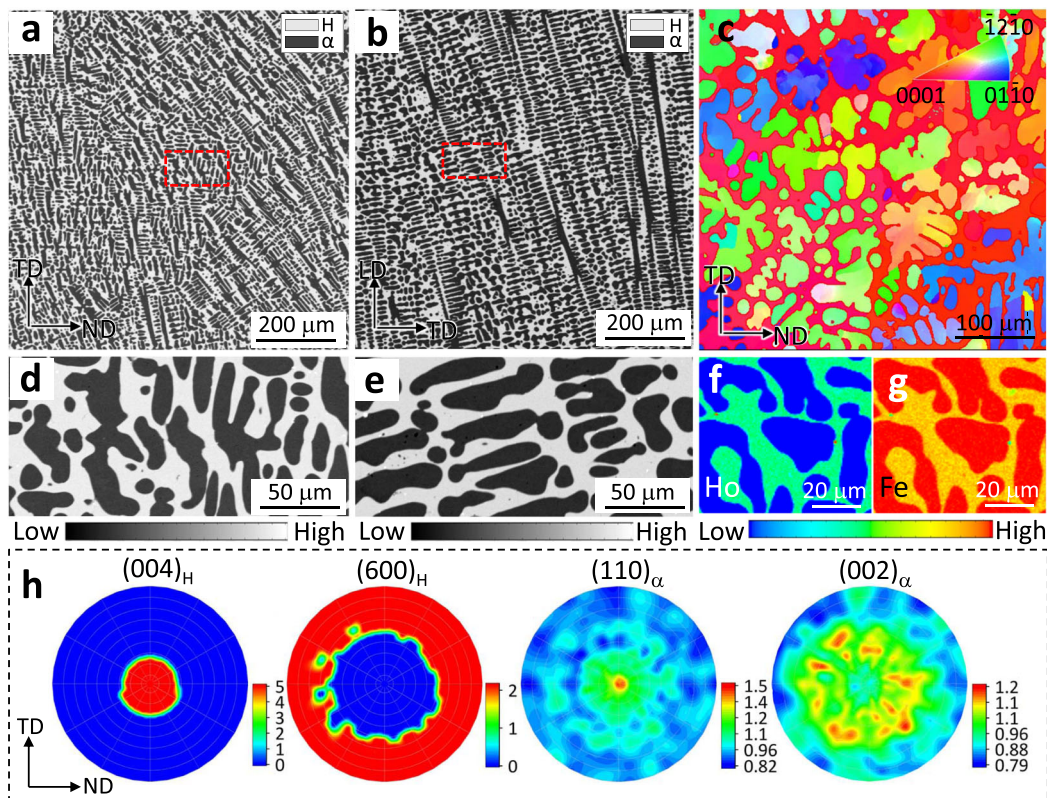


**Fig. 2** Microstructures of the ZTE alloy. **a-b** The morphology of the as-cast S-4 alloy confirmed by electro-probe microanalyzer (EPMA) in TD (transverse direction)-ND (normal direction) plane (**a**) and LD (loading direction)-TD plane (**b**), respectively. (**d**) and (**e**) are enlarged regions in (**a**) and (**b**) marked with a red box. **c** Electron back-scattered diffraction (EBSD) inverse pole figure of crystal orientation for S-4 inside the TD-ND plane. **f-g** Element mappings of Ho (**f**) and Fe (**g**). **h** Pole figures by neutron diffraction texture analysis for the bulk orientations of  $(004)_H$ ,  $(600)_H$ ,  $(110)_\alpha$ , and  $(002)_\alpha$  directions.

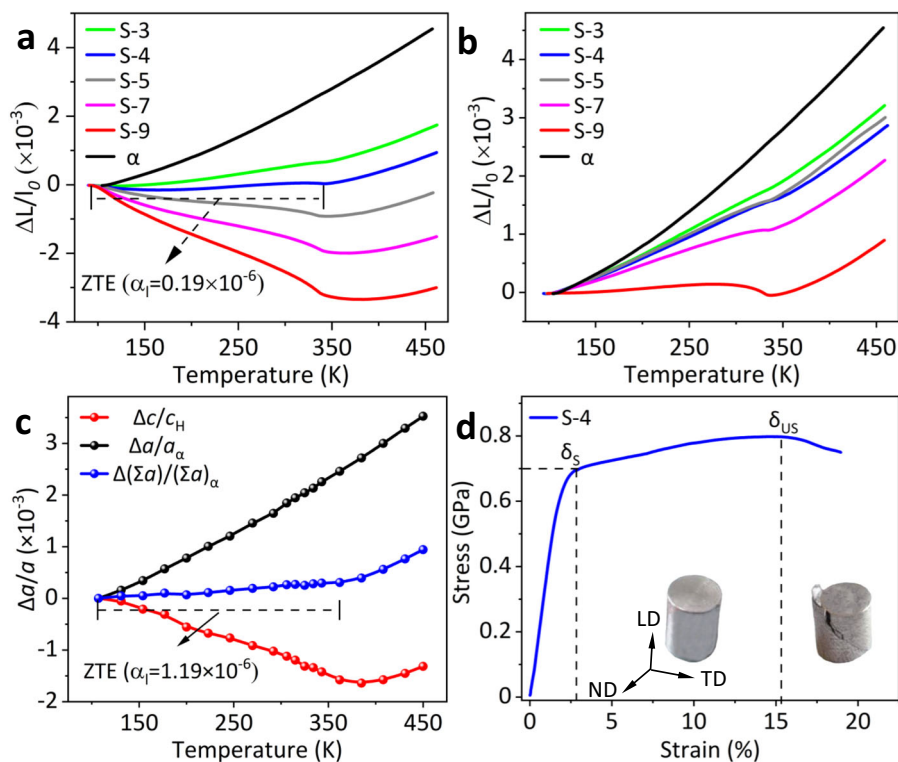


**Fig. 3 Thermal expansion and mechanical properties.** **a** Linear thermal expansion determined by advanced thermo-dilatometer for S-3 to S-9 and iron along with LD. **b** The in-plane (TD-ND) linear thermal expansion of S-3 to S-9 and iron. **c** Lattice thermal expansions of  $\alpha$  along the  $a$  axis, H along the  $c$  axis, and S-4 along with LD. **d** Compressive stress-strain curves of the S-4 with the insets of S-4 ingot during loading.

compressive loading, as shown in the engineering stress-strain curve in Fig. 3d. The ultimate compressive stress ( $\delta_{US}$ ) is up to  $0.80 \pm 0.02$  GPa and the alloy undergoes almost 15.5% compressive strain with an obvious strain-hardening before failure. We note that although S-9 shows ZTE performance in the ND-TD plane, this alloy is brittle with low strength ( $\delta_{US} = 0.41 \pm 0.01$  GPa, see Supplementary Fig. 7), similar to many other ZTE intermetallic compounds<sup>5–11</sup>. Thereafter, the S-4 alloy will be comprehensively discussed because of its ZTE behavior and plasticity. To date, such a high strength-plasticity combination has been scarcely achieved among known ZTE or low thermal expansion (LTE) metallic materials<sup>5–12,15,18</sup>.

## Discussion

To shed light on the mechanism for enhanced strength and plasticity in the ZTE alloy, we investigated the co-deformation process of the two phases by in-situ neutron diffraction measurements under uniaxial compression<sup>29,30</sup> (see Supplementary Fig. 8). Two sets of neutron diffraction patterns were simultaneously recorded in the longitudinal direction (LD, along loading direction) and transverse direction (TD, perpendicular to loading direction) upon loading (see Supplementary Fig. 9). The dramatic difference in peak intensities between LD and TD directions for both the H and the  $\alpha$  phases is caused by fiber texture in the samples, in agreement with previous microstructure analysis (Figs. 4a and 4b). The lattice strain evolution with applied axial strain includes three stages (see Fig. 4c): the soft  $\alpha$  and brittle H phases co-deformed elastically in stage I; the  $\alpha$  phase deformed plastically and the H phase still maintained elastically in stage II, the  $\alpha$  phase yielded at about 0.15 GPa, which is consistent with the behavior of pure  $\alpha$ -Fe, indicating that the H phase has little effect on its yielding behavior (see Supplementary Fig. 10); eventually, co-deformed plastically in stage III.

Figure 4c demonstrates that the interplanar space of  $(004)_H$  can be continuously compressed by increasing engineering strain up

to  $-4.4\%$ , corresponding to the elastic deformation of the H phase at stage II along with a gradually yielding of the  $\alpha$  phase. We extracted the interaction between the soft  $\alpha$  and the brittle H phases by illustrating the full width at half maximum (FWHM) of the reflections (Fig. 4d): the slightly broadening of  $(110)_L$  and  $(110)_T$  in the  $\alpha$  phase corresponds to dislocations generation during yielding (L and T represent LD and TD, respectively); however, the prominently broadening of  $(004)_L$  in the H phase during elastic deformation corresponds to the accumulation of large local strain gradient along with the nucleation of shear bands. It should be emphasized that although both phases yielded and plastically deformed in stage III, the  $\text{Th}_2\text{Ni}_{17}$ -type H phase with large unit cell ( $V = 514.09 \pm 0.03 \text{ \AA}^3$ ) and low symmetry ( $P6_3/mmc$ ) lacks enough independent slip systems for plastic deformation. In fact, the plasticity of the H phase in Stage III is driven by the shear band mechanism<sup>21,31–35</sup> (see Supplementary Fig. 11). This is verified by the asymmetric appearance of the  $\{001\}_H$  reflections along with LD in this stage (arrows in Fig. 4a and Supplementary Fig. 12)—there exist widespread lattice strains caused by shear bands. That is, the lamellar morphology from the eutectic reaction enhances the alloys' mechanical performance via dual-phase synergetic interaction<sup>20,23,31,36–39</sup>.

Phase interface also plays an important role in the enhanced mechanical behaviors and thermal cycling stability<sup>40–42</sup>. High-resolution TEM reveals a  $\sim 1$  nm thick disordered transition layer at the interfaces as shown in Figs. 5a and 5b, two typical interfacial morphologies. The orientation relationship at these interfaces are  $\angle([110]_\alpha, [001]_H) = 34.7^\circ$  and  $[112]_\alpha // [001]_H$  (Figs. 5c and 5d), respectively, implying that there exist some extent of semi-coherent lattice matching between the two phases. The transition layers connect H and  $\alpha$  phases via chemical bonding, minimalizing interfacial energy and giving rise to strong interface linkage and stable thermal cycling performance<sup>43,44</sup>. The thermal cycling test shows that the dual-phase ZTE alloys remain in

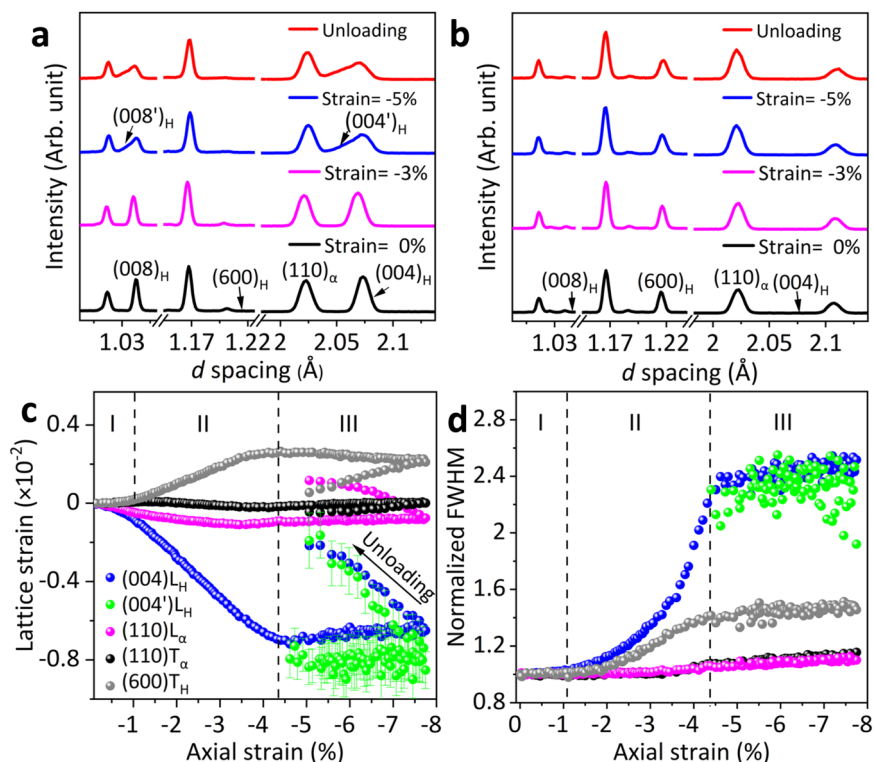


**Fig. 4** Real-time in-situ neutron diffraction studies of S-4 alloy. **a, b** In-situ neutron diffraction profiles at the strain of 0%, -3%, -5%, and unloading stage collected in the LD (**a**) and TD (**b**), respectively, correspond to I, II, and III stages. **c, d** Lattice strains (**c**) and normalized peak FWHMs (**d**) in LD and TD versus applied compressive strain, respectively.

perfect integrity after hundreds of rapid switching between 77 K and 335 K (see Supplementary Fig. 13). Besides, the high elastic strain energy of the brittle H phase can be effectively transferred to the soft  $\alpha$  phase upon loading, and be relieved via dislocation multiplication in the soft and plastic  $\alpha$  phase. This improves the alloy's thermal cycling performance and mechanical stability. Figure 5f demonstrates a typical shear band in the H phase (along loading direction) after -5% deformation, where the lattice constant  $c$  near the shear band at region A (8.46 Å) is smaller than that away from it at region B (8.57 Å). The heterogeneous lattice strain in the H phase (see Figs. 5e–3g) caused by interface interaction accounts for the asymmetric change of the  $\{001\}_H$  reflections obtained by in situ neutron diffraction (Fig. 4a).

This dual-phase synergistic interaction mediated by interface was further demonstrated by ex-situ microstructure studies. After -12% deformation, the localized shear micro-cracks in the brittle H phase are inhibited by the soft  $\alpha$  phase due to its lamellar structure (see Supplementary Fig. 11). Hence, the  $\alpha$  dendrites act as obstacles hindering the excessive deformation of the H phase by pinning the highly localized shear micro-cracks. Meanwhile, substantial dislocations generate in the plastic  $\alpha$  phase after deformation to -12% strain (see Supplementary Fig. 14), which eliminates the stress concentration of the hard H phase and makes it plastic and robust. With further strain increase, the micro-cracks divide into sub-micro-cracks along phase boundaries and lead to shear failure by the adjacent micro-crack penetration (see Supplementary Fig. 15). These results illustrate that the dual-phase alloy undergoes large deformation by absorbing a large amount of work from fracturing, which improves the overall toughness and brings plasticity to the dual-phase alloy.

For comparison, in Fig. 6a we summarized ultimate strain versus compressive strength and ZTE temperature range ( $\Delta T$ ) for

the ZTE alloy S-4, and other typical ZTE or near ZTE metallic materials<sup>5,7,8,11,12,15,18,45–49</sup>. ZTE intermetallic compounds are of low strength and high brittleness though they possess desired ZTE performance. For traditional La(Fe,Si)<sub>13</sub>-based composites, their strengths are high but have little plasticity and their ZTE is mostly limited in a narrow temperature range. Er-Fe-V-Mo dual-phase alloy has high strength and wide near ZTE temperature range, but has no plasticity. In contrast, the present dual-phase ZTE alloy S-4 shows a favorable strength-plasticity combination and a considerable wide ZTE temperature range ( $\Delta T = 235$  K) and is much stronger than the widely used Invar alloy at comparable strains. Most importantly, this ZTE alloy S-4 is easy to machine and can be fabricated to various structures, such as precision gears against thermal shock and sealing ring enduring temperature fluctuation, etc., with stable thermal cycling performance (see Fig. 6b and Supplementary Fig. 5). We also emphasize that the present Fe-based ZTE alloy contains only 4 at.% rare-earth Ho, making it cost-effective with great application potentials (see Supplementary Fig. 16).

In summary, we used the eutectic reaction method to overcome the contradiction between ZTE and plasticity in metallic materials. By this method, we successfully designed and fabricated a Fe-based ZTE dual-phase alloy, Ho<sub>0.04</sub>Fe<sub>0.96</sub>, with a combination of low-cost, stable thermal cycling performance, and moderate strength-plasticity. The lamellar dual-phase microstructure with the semi-coherent interface not only regulates the thermal expansion behavior but also greatly enhances the mechanical properties and improves the thermal stability of the Fe-based ZTE alloy. The comprehensive performance of the present dual-phase alloy may effectively avoid the “Buckets Effect” caused by the imbalance of material properties, endowing it a broad application prospect. We expect that more high-performance ZTE alloys could be developed by using the eutectic reaction strategy.

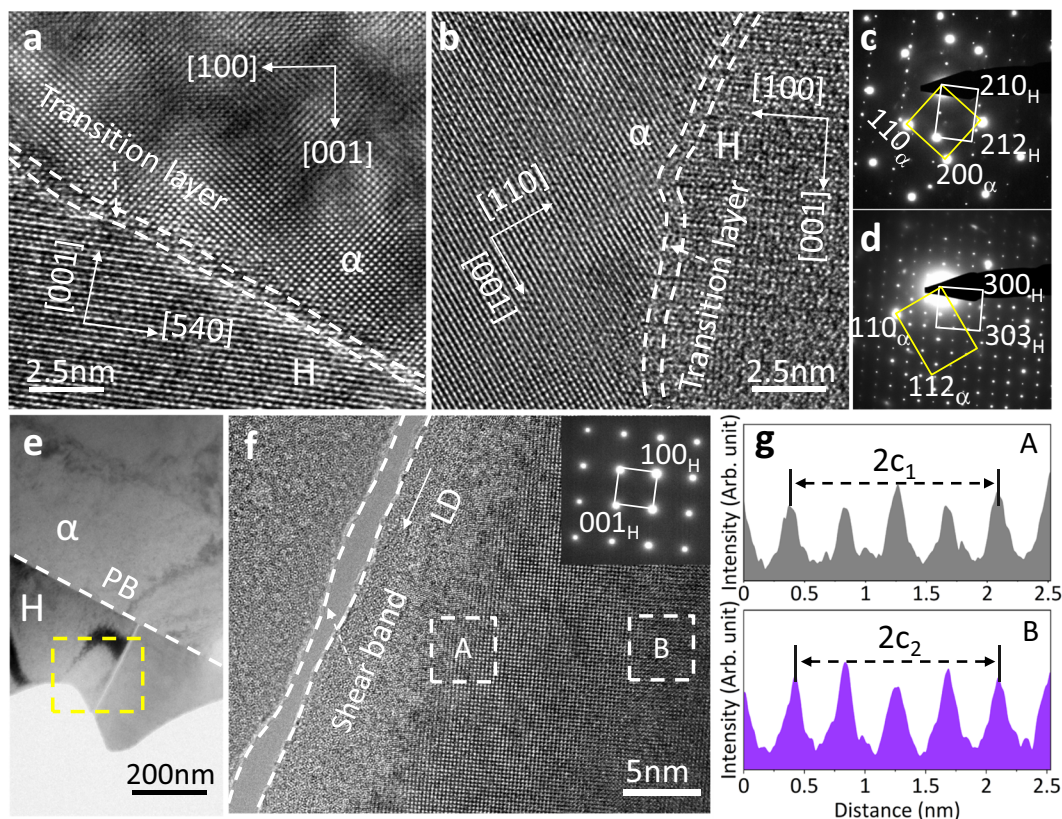


**Fig. 5** TEM studies of S-4 alloy. **a, b** High-resolution transmission electron microscopy (HRTEM) image at the phase interface, oriented to the  $[001]_{\alpha}$  zone axis (**a**) and  $[\bar{1}\bar{1}0]_{\alpha}$  zone axis (**b**), respectively. **c, d** Selected area electron diffraction (SAED) at the phase interface correspond to Fig. 5a and b, respectively. **e** The microstructure of the S-4 alloy at the strain of  $-5\%$  along the loading direction, the white dashed line indicates the phase boundary (PB). **f** The HRTEM image at the shear band area of the H phase, insert is the SAED at the H phase, oriented to the  $[010]$  zone axis. The local shear band is formed after large compressive deformation. **g** Intensity profile along with LD in A and B zones marked in Fig. 5f.

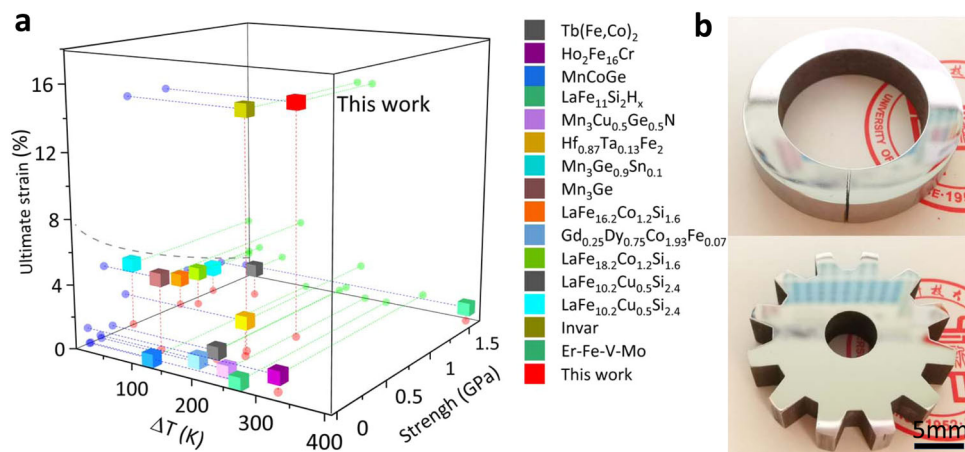


**Fig. 6** Summary of mechanical and thermal expansion performance. **a** A review of critical parameters for the typical (near) zero thermal expansion metallic materials: ultimate strain, strength, and temperature window. Note: Invar is a completely plastic material, for comparison, we used the compressive strength at  $15.6\%$  strains here. **b** Pictures of gear (up) and sealing (down) ring fabricated by the present ZTE alloy (S-4).

## Methods

**Synthesis methods.** The samples of  $\text{Ho}_x\text{Fe}_{1-x}$  ( $x = 0.03$ ,  $x = 0.04$ ,  $x = 0.05$ ,  $x = 0.07$ ,  $x = 0.09$ , labeled as S-3, S-4, S-5, S-7, S-9) were prepared the constituent elements, Ho and Fe ( $>99.9\%$  purity) by a vacuum arc melting furnace under high purity argon atmosphere. The samples were turned over and melted four times to ensure homogeneity. Then, the sample was followed by annealing at  $1373\text{ K}$  in an argon atmosphere for about  $24\text{ h}$  and quenched in water.

**SXRD measurements.** The ambient temperature ( $\lambda = 0.23991\text{ \AA}$ ) and in-situ SXRD measurements ( $\lambda = 0.45\text{ \AA}$ ) of the samples were performed at the SPring-8,

Japan. The phase structures and fractions were obtained by Rietveld refinements with FULLPROF software.

**EPMA measurements.** The phase contrast and microstructure analysis were measured by electro-probe microanalyzer backscattering electron (EPMA-BSE) spectrum (SHIMADZU 1720) equipped with wave-length dispersive spectrometer analysis (WDS) to quantitative determine the phase composition.

**SEM and EBSD measurements.** The surface of fracture and the microstructure orientation of the samples were measured by scanning electron microscope (SEM),

Zeiss GeminiSEM 500), electron backscattering diffraction (EBSD, TESCAN MIRA 3 LMH SEM, and Symmetry EBSD).

**TEM measurements.** The microstructure of the as-cast sample was characterized by the high-resolution transmission electron microscopy (HRTEM) and was measured by an aberration-corrected FEI Titan G260–300 kV S/TEM. All pictures were handled with Gatan Digital Micrograph software.

**Linear thermal expansion of the alloy.** The linear thermal expansion curves ( $\Delta L/L_0$ ) were measured by an advanced thermo-dilatometer (NETZSCH DIL402) with a heating rate of 5 K/min.

**Mechanical properties.** The sample was fabricated into  $\Phi 6 \times 8$  mm cylinder by electrical discharging. At least 5 samples were tested for each composition. The room-temperature mechanical properties were measured using a CMT4105 universal electronic compressive testing machine with an initial strain rate of  $7.0 \times 10^{-4} \text{ s}^{-1}$ .

**In situ neutron diffraction measurements.** The real-time in-situ neutron diffraction experiments were carried out at VULCAN beamline in Oak Ridge National Laboratory<sup>29,50</sup> (ORNL), USA. All the lattice strain during the compressive is determined by the single peak fitting method for the (h,k,l) reflections. The lattice strain was calculated by following formula (Eq. 1):

$$\text{Strain} = (d_1 - d_0)/d_0 \times 100\% \quad (1)$$

Here  $d_1$  and  $d_0$  represent the interplanar crystal spacing of the (hkl) crystal plane after and before loading, respectively.

**The lattice thermal expansion of the dual-phase alloy.** The lattice thermal expansion of dual-phase alloy was calculated as (Eq. 2) and (Eq. 3):

$$\alpha_{S-4} = \frac{\Sigma \alpha_1 - \Sigma \alpha_0}{\Sigma \alpha_0} / (T_1 - T_0) \quad (2)$$

$$\Sigma \alpha = \text{mol.}_\alpha\% \times \alpha_\alpha + \text{mol.}_H\% \times \alpha_H \quad (3)$$

where  $\alpha_{S-4}$  is the corrected CTEs along with the LD for S-4;  $\text{mol.}_\alpha\%$  and  $\text{mol.}_H\%$  are molar fractions of  $\alpha$  and H determined by the results of SXRD data. Due to the high crystallographic texture of the S-4 with  $\langle 001 \rangle$ /LD and the homogeneous lamellar microstructure, we use the  $c$  axis of the H phase,  $a$  axis for the  $\alpha$  phase, and molar fractions to calculate the overall thermal expansion along with the LD.

**Thermal cycling test.** To determine the thermal cycling stability of the dual-phase alloys caused by the mismatch of CTEs between the two phases, a thermal-cycling test was conducted by an auto-mechanical arm. The sample was submerged in liquid nitrogen (77 K) for 10 s and then quickly transferred to hot water (335 K) and kept for another 10s, which is the whole cycle.

## Data availability

The data that support the findings of this study are available from the corresponding authors upon reasonable request.

Received: 30 December 2020; Accepted: 17 June 2021;

Published online: 04 August 2021

## References

- Mohn, P. A century of zero expansion. *Nature* **400**, 18–19 (1999).
- Zheng, X. et al. Giant negative thermal expansion in magnetic nanocrystals. *Nat. Nanotechnol.* **3**, 724–726 (2008).
- Salvador, J. et al. Zero thermal expansion in YbGaGe due to an electronic valence transition. *Nature* **425**, 702–704 (2003).
- Song, Y. et al. Magnetic-field-induced strong negative thermal expansion in La(Fe,Al)<sub>13</sub>. *Chem. Mater.* **32**, 7535–7541 (2020).
- Hu, J. et al. Adjustable magnetic phase transition inducing unusual zero thermal expansion in cubic RCo<sub>2</sub>-based intermetallic compounds (R = Rare Earth). *Inorg. Chem.* **58**, 5401–5405 (2019).
- Cao, Y. et al. Role of “dumbbell” pairs of Fe in spin alignments and negative thermal expansion of Lu<sub>2</sub>Fe<sub>17</sub>-based intermetallic compounds. *Inorg. Chem.* **59**, 11228–11232 (2020).
- Van Schilfgaarde, M. et al. Origin of the Invar effect in iron-nickel alloys. *Nature* **400**, 4 (1999).
- Song, Y. et al. Zero thermal expansion in magnetic and metallic Tb(Co,Fe)<sub>2</sub> intermetallic compounds. *J. Am. Chem. Soc.* **140**, 602–605 (2018).
- Huang, R. et al. Giant negative thermal expansion in NaZn<sub>13</sub>-type La(Fe, Si, Co)<sub>13</sub> compounds. *J. Am. Chem. Soc.* **135**, 11469–11472 (2013).
- Hu, J. et al. A case of multifunctional intermetallic compound: negative thermal expansion coupling with magnetocaloric effect in (Gd,Ho)(Co,Fe)<sub>2</sub>. *Inorg. Chem. Front.* **6**, 3146–3151 (2019).
- Dan, S., Mukherjee, S., Mazumdar, C. & Ranganathan, R. Zero thermal expansion with high Curie temperature in Ho<sub>2</sub>Fe<sub>16</sub>Cr alloy. *RSC Adv.* **6**, 94809–94814 (2016).
- Zhao, Y. et al. Giant negative thermal expansion in bonded MnCoGe-based compounds with Ni<sub>2</sub>In-type hexagonal structure. *J. Am. Chem. Soc.* **137**, 1746–1749 (2015).
- Li, W. et al. Strong coupling of magnetism and lattice induces near-zero thermal expansion over broad temperature windows in ErFe<sub>10</sub>V<sub>2-x</sub>Mo<sub>x</sub> compounds. *CCS Chem.* **3**, 1009–1015 (2020).
- Guan, Q. et al. Lightweight, tough, and sustainable cellulose nanofiber-derived bulk structural materials with low thermal expansion coefficient. *Sci. Adv.* **6**, 114 (2020).
- Liu, J. et al. Realization of zero thermal expansion in La(Fe,Si)<sub>13</sub>-based system with high mechanical stability. *Mater. Des.* **148**, 71–77 (2018).
- Wu, G. et al. Decomposition of ZrW<sub>2</sub>O<sub>8</sub> in Al matrix and the influence of heat treatment on ZrW<sub>2</sub>O<sub>8</sub>/Al–Si thermal expansion. *Scr. Mater.* **96**, 29–32 (2015).
- Song, Y. et al. Negative thermal expansion in (Sc,Ti)Fe<sub>2</sub> induced by unconventional magnetovolume effect. *Mater. Horiz.* **7**, 275–281 (2019).
- Lin, K. et al. High performance and low thermal expansion in Er-Fe-V-Mo dual-phase alloys. *Acta Mater.* **198**, 271–280 (2020).
- Wang, Y. et al. Enhanced thermal and mechanical properties of Sr<sub>0.2</sub>Ba<sub>0.8</sub>TiO<sub>3</sub>/Cu matrix composites by introducing Cu<sub>2</sub>O interface coating. *Mater. Des.* **166**, 107594 (2019).
- Shi, P. et al. Enhanced strength-ductility synergy in ultrafine-grained eutectic high-entropy alloys by inheriting microstructural lamellae. *Nat. Commun.* **10**, 489 (2019).
- Wu, G., Chan, K., Zhu, L., Sun, L. & Lu, J. Dual-phase nanostructuring as a route to high-strength magnesium alloys. *Nature* **545**, 80–83 (2017).
- Takenaka, K. et al. Colossal negative thermal expansion in reduced layered ruthenate. *Nat. Commun.* **8**, 14102 (2017).
- Pandey, P. et al. On the origin of a remarkable increase in the strength and stability of an Al rich Al–Ni eutectic alloy by Zr addition. *Acta Mater.* **170**, 205–217 (2019).
- Sheng, L., Guo, J. & Ye, H. Microstructure and mechanical properties of NiAl–Cr(Mo)/Nb eutectic alloy prepared by injection-casting. *Mater. Des.* **30**, 964–969 (2009).
- Wang, X. et al. Solidified microstructures and elastic modulus of hypo-eutectic and hyper-eutectic TiB<sub>2</sub>-reinforced high-modulus steel. *Acta Mater.* **176**, 84–95 (2019).
- Roe, G. & O’keefe, T. The Fe–Ho binary system. *Metall. Trans.* **1**, 3 (1970).
- Cao, Y. et al. Manipulating spin alignments of (Y,Lu)<sub>1.7</sub>Fe<sub>17</sub> intermetallic compounds via unusual thermal pressure. *Inorg. Chem.* **59**, 5247–5251 (2020).
- Cao, Y. et al. Neutron diffraction study of unusual magnetic behaviors in the Ho<sub>2</sub>Fe<sub>11</sub>Al<sub>6</sub> intermetallic compound. *Inorg. Chem.* **58**, 13742–13745 (2019).
- An, K. et al. First in situ lattice strains measurements under load at VULCAN. *Metall. Mater. Trans. A* **42**, 95–99 (2011).
- Beese, A. et al. Absence of dynamic strain aging in an additively manufactured nickel-base superalloy. *Nat. Commun.* **9**, 2083 (2018).
- Ma, Y. et al. Phase boundary segregation-induced strengthening and discontinuous yielding in ultrafine-grained duplex medium-Mn steels. *Acta Mater.* **200**, 389–403 (2020).
- Jiang, S. et al. Micromechanical behavior of multilayered Ti/Nb composites processed by accumulative roll bonding: An in-situ synchrotron X-ray diffraction investigation. *Acta Mater.* **205**, 116546 (2021).
- He, G., Eckert, J., Loser, W. & Schultz, L. Novel Ti-base nanostructure-dendrite composite with enhanced plasticity. *Nat. Mater.* **2**, 33–37 (2003).
- Inoue, A., Shen, B., Koshihara, H., Kato, H. & Yavari, A. Cobalt-based bulk glassy alloy with ultrahigh strength and soft magnetic properties. *Nat. Mater.* **2**, 661–663 (2003).
- Hofmann, D. et al. Designing metallic glass matrix composites with high toughness and tensile ductility. *Nature* **451**, 1085–1089 (2008).
- Jin, X. et al. A new CrFeNiAl eutectic high entropy alloy system with excellent mechanical properties. *J. Alloy. Compd.* **770**, 655–661 (2019).
- Su, J., Raabe, D. & Li, Z. Hierarchical microstructure design to tune the mechanical behavior of an interstitial TRIP-TWIP high-entropy alloy. *Acta Mater.* **163**, 40–54 (2019).
- Bei, H. & George, E. Microstructures and mechanical properties of a directionally solidified NiAl–Mo eutectic alloy. *Acta Mater.* **53**, 69–77 (2005).
- Kim, S., Kim, H. & Kim, N. Brittle intermetallic compound makes ultrastrong low-density steel with large ductility. *Nature* **518**, 77–79 (2015).
- Ding, R. et al. Chemical boundary engineering: A new route toward lean, ultrastrong yet ductile steels. *Sci. Adv.* **6**, 1430 (2020).

41. Lu, K., Lu, L. & Suresh, S. Strengthening materials by engineering coherent internal boundaries at the nanoscale. *Science* **324**, 4 (2009).
42. Lu, L., Chen, X., Huang, X. & Lu, K. Revealing the maximum strength in nanotwinned copper. *Science* **323**, 4 (2009).
43. Sun, L., Irving, D., Zikry, M. & Brenner, D. First-principles investigation of the structure and synergistic chemical bonding of Ag and Mg at the Al| $\Omega$  interface in a Al–Cu–Mg–Ag alloy. *Acta Mater.* **57**, 3522–3528 (2009).
44. Liu, J. et al. Understanding chemical bonding in alloys and the representation in atomistic simulations. *J. Phys. Chem. C* **122**, 14996–15009 (2018).
45. Li, S. et al. Zero thermal expansion achieved by an electrolytic hydriding method in La(Fe,Si)<sub>13</sub> compounds. *Adv. Funct. Mater.* **27**, 1604195 (2017).
46. Nakamura, Y., Takenaka, K., Kishimoto, A. & Takagi, H. Mechanical properties of metallic perovskite Mn<sub>3</sub>Cu<sub>0.5</sub>Ge<sub>0.5</sub>N: high-stiffness isotropic negative thermal expansion material. *J. Am. Ceram. Soc.* **92**, 2999–3003 (2009).
47. Li, L. et al. Good comprehensive performance of Laves phase Hf<sub>1-x</sub>Ta<sub>x</sub>Fe<sub>2</sub> as negative thermal expansion materials. *Acta Mater.* **161**, 258–265 (2018).
48. Song, Y. et al. Opposite thermal expansion in isostructural noncollinear antiferromagnetic compounds of Mn<sub>3</sub>A (A = Ge and Sn). *Chem. Mater.* **30**, 6236–6241 (2018).
49. Wang, J. et al. Balancing negative and positive thermal expansion effect in dual-phase La(Fe,Si)<sub>13</sub>/ $\alpha$ -Fe in-situ composite with improved compressive strength. *J. Alloy. Compd.* **769**, 233–238 (2018).
50. An, K., Chen, Y. & Stoica, D. A. VULCAN: a “hammer” for high-temperature materials research. *MRS Bull.* **44**, 878–883 (2019).

## Acknowledgements

This research was supported by National Key R&D Program of China (2020YFA0406200), National Natural Science Foundation of China (22090042 and 21731001, 21971009), and the Fundamental Research Funds for the Central Universities, China (FRF-IDRY-19-018, FRF-BR-19-003B), and National Postdoctoral Program for Innovative Talents (BX201700027). The synchrotron radiation experiments were performed at the BL02B2 and BL44B2 of SPring-8 with the approval of the Japan Synchrotron Radiation Research Institute (JASRI) (Proposal No. 2018B1306, 2018B1515); Neutron diffraction work was carried out at the Spallation Neutron Source (SNS) (Proposal No. 21913, 26069), which is the U.S. Department of Energy (DOE) user facility at the Oak Ridge National Laboratory, sponsored by the Scientific User Facilities Division, Office of Basic Energy Sciences. The authors thank Mr. M. J. Frost at SNS for technical support.

## Author contributions

C.Y.Y. and K.L. designed the study. C.Y.Y. carried out the main experiments. C.Y.Y., K.L., and X.R.X. analyzed the data and wrote the main draft of the paper. S.H.J. analyzed the mechanical behavior of the sample. J.C., J.X.D., W.J.L., Y.L.C., and Y.L.W. analyzed the thermal expansion results. Q.L., Y.C., and K.A. analyzed the in situ neutron diffraction results. L.Y. conducted the TEM characterization. K.K. conducted the SXRD measurements. All authors discussed the results and commented on the manuscript.

## Competing interests

The authors declare no competing interests.

## Additional information

**Supplementary information** The online version contains supplementary material available at <https://doi.org/10.1038/s41467-021-25036-1>.

**Correspondence** and requests for materials should be addressed to K.L. or X.X.

**Peer review information** *Nature Communications* thanks the anonymous reviewers for their contribution to the peer review of this work.

**Reprints and permission information** is available at <http://www.nature.com/reprints>

**Publisher's note** Springer Nature remains neutral with regard to jurisdictional claims in published maps and institutional affiliations.



**Open Access** This article is licensed under a Creative Commons

Attribution 4.0 International License, which permits use, sharing, adaptation, distribution and reproduction in any medium or format, as long as you give appropriate credit to the original author(s) and the source, provide a link to the Creative Commons license, and indicate if changes were made. The images or other third party material in this article are included in the article's Creative Commons license, unless indicated otherwise in a credit line to the material. If material is not included in the article's Creative Commons license and your intended use is not permitted by statutory regulation or exceeds the permitted use, you will need to obtain permission directly from the copyright holder. To view a copy of this license, visit <http://creativecommons.org/licenses/by/4.0/>.

© The Author(s) 2021